

A semi-analytical beam model for the vibration of railway tracks

D. Kostovasilis, D.J. Thompson and M.F.M. Hussein

Journal: Journal of Sound and Vibration

Received: 23 May 2016

Revised: 6 Nov 2016

Accepted: 20 Dec 2016

DOI: <http://doi.org/10.1016/j.jsv.2016.12.033>

ePrints URL: <http://eprints.soton.ac.uk/404109/>

Data DOI: <http://doi.org/10.5258/SOTON/404573>

A semi-analytical beam model for the vibration of railway tracks

D. Kostovasilis*, D.J. Thompson

*Institute of Sound and Vibration Research, University of Southampton, Highfield Campus, Southampton,
SO17 1BJ, United Kingdom*

M.F.M. Hussein

*Department of Civil and Architectural Engineering, College of Engineering, University of Qatar, P.O. Box
2713, Doha, Qatar*

Abstract

The high frequency dynamic behaviour of railway tracks, in both vertical and lateral directions, strongly affects the generation of rolling noise as well as other phenomena such as rail corrugation. An improved semi-analytical model of a beam on an elastic foundation is introduced that accounts for the coupling of the vertical and lateral vibration. The model includes the effects of cross-section asymmetry, shear deformation, rotational inertia and restrained warping. Consideration is given to the fact that the loads at the rail head, as well as those exerted by the railpads at the rail foot, may not act through the centroid of the section. The response is evaluated for a harmonic load and the solution is obtained in the wavenumber domain. Results are presented as dispersion curves for free and supported rails and are validated with the aid of a Finite Element (FE) and a waveguide finite element (WFE) model. Closed form expressions are derived for the forced response, and validated against the WFE model. Track mobilities and decay rates are presented to assess the potential implications for rolling noise and the influence of the various sources of vertical-lateral coupling. Comparison is also made with measured data. Overall, the model presented performs very well, especially for the lateral vibration, although it does not contain the high frequency cross-section deformation modes. The most significant effects on the response are shown to be the inclusion of torsion and foundation eccentricity, which mainly affect the lateral response.

Keywords: Vertical/lateral coupling, dispersion curve, Vignole rail, 60E1, frequency-wavenumber domain

*Corresponding author: Email: d.kostovasilis@hud.ac.uk
Now at Institute of Railway Research, University of Huddersfield, Queensgate, Huddersfield, HD1 3DH

1. Introduction

The dynamic behaviour of railway tracks at high frequencies and their sound radiation characteristics are particularly important for the generation of rolling noise as well as other phenomena such as rail corrugation. The track vibration in both vertical and lateral directions contributes to the radiated noise. The excitation due to the surface roughness is vertical. However, as pointed out by Vincent et al. [1], the relative contribution of vertical and lateral components relies mainly on the location of the contact between the wheel and rail and on the attenuation of the respective waves along the rail. Typically the attenuation of the lateral waves is lower, and if there is a significant offset of the contact, the sound power due to lateral vibration may reach and even exceed the vertical component. Thus it is important to account for the rail radiation due to lateral/torsional waves in the rail. Many authors use analytical or semi-analytical models and focus mainly on the vertical track vibration but the lateral vibration, and especially the coupling of the vertical and lateral directions, have received much less attention [2].

By comparing experimental results of the lateral track receptance (displacement due to a unit force) with the results of vertical track dynamic models, Grassie et al. [3] suggested that the latter could be adapted to represent the lateral response. For stiffer railpads (on wooden sleepers) good agreement was obtained between the measurements and a dynamic model of a beam on an elastic foundation, whereas for softer railpads (modern track with concrete sleepers) it was found that the rail head undergoes large lateral bending vibration, independent of that of the foot, the web itself acting as an elastic foundation. They thus used a two-layer continuous foundation model accounting for the rail head (as a Timoshenko beam) connected by a series of springs to the rail foot (continuous mass) and further connected to the second elastic layer representing the pads. Good agreement was found between this model and measurements of the track lateral receptance.

In the works of Thompson et al. [4, 5, 6], both vertical and lateral track behaviour was considered using a Timoshenko beam on a two-layer foundation model. This led to an underprediction of the lateral receptance due to the neglect of torsion. An empirical parameter was introduced (X) to allow for the cross-coupling between vertical and lateral directions. The cross receptance (receptance in one direction due to a unit force in another direction) was estimated from the geometrical average of the vertical (A_y) and lateral (A_z) receptances ($A_{yz} = X\sqrt{A_y A_z}$), where X was obtained by comparison with measurements.

Wu and Thompson [7, 8] developed continuously supported multiple beam models for both vertical and lateral vibration, which included cross-sectional deformation in an approximate way. Although they showed excellent agreement with a finite element (FE) model in terms of dispersion characteristics (wavenumber plotted against frequency), the effect of vertical-lateral coupling was not considered.

Thompson [9] obtained the dispersion relationship and receptance of an infinite rail based on the periodic structure theory (PST) of Mead [10]. This technique takes advantage of the fact that the cross-section remains constant along the rail and that its length is infinite. The structure is considered as a periodic structure with arbitrary period. A slice of rail 10 mm long was discretised by finite elements (FE), and the sleepers were also included in

an equivalent continuously supported model. In this method, a commercial finite element software can be used to obtain the FE matrices.

The finite strip method was used by Knothe et al. [11], where only the cross-section of the rail was discretised and the elements were considered as infinite strips. The main advantages of this method over classical Finite Element Analysis are the reduced number of degrees of freedom, thus decreasing computational requirements and the avoidance of truncation effects at the end of the finite section of rail. Similarly, Gavrić [12] introduced the waveguide finite element (WFE) method for modelling of rails. In this method, as with the PST method, the infinite extent of the rail and the constant cross-section are taken into account. The cross-section is modelled using special two-dimensional finite elements, similar to the finite strip method. The displacement field across the cross-section is discretised by finite elements while complex exponentials are used to describe the waves in the longitudinal direction. Results were presented in the form of the dispersion of free waves propagating in an unsupported rail. Using the same approach, Ryue et al. [13] determined the waves propagating in a supported rail up to 80 kHz. Nilsson et al. [14] used the waveguide finite element method to calculate the vibration of an infinite, continuously supported rail excited by a point force. The forced response was also obtained by Gry [15] for a rail with periodic supports.

Bhaskar et al. [16] developed an analytical model accounting for the lateral and rotational motion of the rail. The frequency range of interest in this work was up to about 2000 Hz, thus it was considered important to account for the cross-sectional deformation occurring above 1500 Hz. The authors based their model on a finite element model developed by Ripke and Knothe [17] where the rail section is composed by three separate parts, representing the rail head as a beam in bending and torsion, and the rail web and foot by three plates (one for the web and one for the foot on each side of the web). A variational method was then used to obtain a model for an infinite rail continuously supported on railpads, sleepers and ballast in order to obtain the dispersion relationship and receptance. The rail head was allowed to translate in vertical, axial and lateral directions, as well as to rotate around the axial direction. The plates were allowed displacement in plane as well as deformation perpendicular to their plane. The railpads were represented by two springs set a distance apart equal to the width of the foot divided by $\sqrt{3}$ to account for the torsional stiffness as well. The responses of the rail were also obtained by means of Fourier integrals. A good agreement was found with the discretely supported finite element model developed by Ripke and Knothe [17], with the main differences occurring due to the continuous nature of the support.

In an attempt to understand and quantify the vertical-lateral coupling of rails, Betgen et al. [18] analysed the track mobility and decay rates by means of measurements and a Finite Element model and these were compared with the analytical models of Thompson et al. [6]. The rail was excited vertically at various locations across the top of the railhead and laterally at the side of the railhead. It was shown that the simplified Timoshenko beam models fail to capture many important characteristics of the response and that the cross mobility is significantly affected by the lateral position of the vertical force. The influence of

asymmetry of the sleeper was found to be minimal, while the value of 0.3 (-10 dB) typically used for the factor X in the TWINS model was found to give reasonably good results for a lateral offset of 20 mm.

The main disadvantage of these numerical methods is that they require more extensive computational capacity and increased calculation times compared with analytical or semi-analytical models. Thus an analytical approach could be of great benefit, depending on the required level of accuracy and application. Moreover, an analytical model has the advantage of offering increased physical insight. In the present work, a semi-analytical approach is used to consider the various sources of vertical/lateral interaction. Cross-section deformation is not taken into account but instead the rail is treated as a simple beam cross-section, accounting for vertical and lateral bending, extension and torsion. Corrections for shear deformation, shear centre eccentricity and warping are included. The dispersion relationship is compared with results from a WFE model. The potential implications for rolling noise of the various sources of vertical/lateral coupling are presented in terms of the track decay rates. The main aim of this work is to provide insight into the relative importance of the various coupling effects that exist for railway applications.

In the following section, the track model will be presented and validated, followed by a study of the forced response. Finally the model is compared with measurements performed on a test track.

2. Rail model

2.1. Equations of motion

For mainline tracks, the usual unworn Vignole rail section is symmetric about its vertical mid-plane but is asymmetric about the horizontal mid-plane. As a result, the shear centre, through which the shear forces can be considered to act, is not coincident with the centroid through which inertial forces are considered to act. This introduces a coupling between lateral bending and torsion. For a fully asymmetric section, such as a groove tram rail, the same will occur between vertical bending and torsion, although to a lesser extent.

Figure 1 shows a typical rail cross-section for mainline track, where C denotes the centroid and S the shear centre, e_y being the distance between them in the vertical (y) direction, while in the lateral (z) direction it is $e_z=0$. The positions 1-4 shown on the rail head are the force locations used in later sections.

The dynamic track model adopted is based on a static beam model presented by Kim et al. [19] for the stability of beam columns. This utilises Timoshenko beam theory for bending in the vertical and lateral directions, an axial rod in extension and a torsional rod. The model also accounts for shear-centre eccentricity and non-uniform torsion. This model has been extended here to include inertial effects and an elastic support at an arbitrary location relative to the centroid. By considering the generalised displacement field, the linear components of the strains in Cartesian co-ordinates can be derived as well as the strain/displacement equations. In this work, higher order terms of displacements are neglected. Moreover, the support stiffness is assumed to be linear. This is due to the fact that the vibration amplitudes are small so non-linearities can be ignored. Assuming a linear

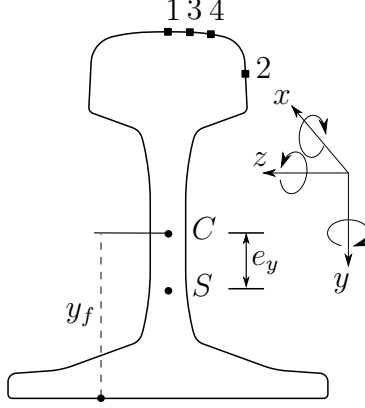


Figure 1: Rail cross-section profile for 60E1. Positions 1-4 are force locations.

elastic isotropic material, the stress-strain relationships can be derived based on the constitutive relationships of elasticity. Then, the stress resultants acting on the cross-section can be calculated by integrating the appropriate stresses over the cross-sectional area, for both normal and shear stresses, yielding the force/deformation equations [19].

In order to illustrate the approach, consider first only the vertical bending of the rail. The classical equations of motion for a Timoshenko beam can be derived in the spatial domain as [20]:

$$-GA\kappa_y \left(\frac{\partial^2 u_y}{\partial x^2} - \frac{\partial \theta_z}{\partial x} \right) + k_y u_y + \rho A \frac{\partial^2 u_y}{\partial t^2} = F_y \quad (1)$$

$$-EI_z \frac{\partial^2 \theta_z}{\partial x^2} - GA\kappa_y \left(\frac{\partial u_y}{\partial x} - \theta_z \right) + k_{rz} \theta_z + \rho I_z \frac{\partial^2 \theta_z}{\partial t^2} = M_z \quad (2)$$

where u_y is the displacement in the y direction, θ_z is the rotation around the z axis, F_y and M_z are the external force and moment per unit length applied at the centroid, E and G are the Young's modulus and shear modulus respectively, A is the cross-section area of the rail, κ_y is the shear coefficient for bending in the y direction, ρ is the density of the rail, I_z is the second moment of area around the z axis, x is the axial direction and k_y and k_{rz} are the translational and rotational stiffnesses per unit length derived from the stiffness per pad (i.e. k_y^p) by dividing by the sleeper spacing (i.e. $k_y = k_y^p/l_{sp}$). The above equations of motion can also be written in matrix form as:

$$(\mathbf{K}_p + \mathbf{K}_0) \mathbf{U} + \mathbf{K}_1 \frac{\partial \mathbf{U}}{\partial x} + \mathbf{K}_2 \frac{\partial^2 \mathbf{U}}{\partial x^2} + \mathbf{M} \frac{\partial^2 \mathbf{U}}{\partial t^2} = \mathbf{F} \quad (3)$$

where $\mathbf{U}(x, t)$ is a vector of the two components of vibration (u_y and θ_z) at the centroid.

The matrices \mathbf{K}_p , \mathbf{K}_0 , \mathbf{K}_1 , \mathbf{K}_2 and \mathbf{M} for the Timoshenko beam are given as:

$$\mathbf{K}_p = \begin{bmatrix} k_y & 0 \\ 0 & k_{rz} \end{bmatrix} \quad (4)$$

$$\mathbf{K}_0 = \begin{bmatrix} 0 & 0 \\ 0 & GA\kappa_y \end{bmatrix} \quad (5)$$

$$\mathbf{K}_1 = \begin{bmatrix} 0 & GA\kappa_y \\ -GA\kappa_y & 0 \end{bmatrix} \quad (6)$$

$$\mathbf{K}_2 = \begin{bmatrix} -GA\kappa_y & 0 \\ 0 & -EI_z \end{bmatrix} \quad (7)$$

$$\mathbf{M} = \begin{bmatrix} m & 0 \\ 0 & \rho I_z \end{bmatrix} \quad (8)$$

where \mathbf{K}_p is the support stiffness matrix, \mathbf{K}_0 is the classical (2D) stiffness matrix, \mathbf{K}_1 and \mathbf{K}_2 contain stiffness terms related to the first and second derivatives in the x direction and \mathbf{M} is the inertial matrix.

The responses are assumed to be harmonic both in space and time with circular frequency ω and complex wavenumber ξ as:

$$\mathbf{U} = \tilde{\mathbf{U}} e^{i\omega t} e^{-i\xi x} \quad (9)$$

in which $\tilde{\mathbf{U}}$ is the vector of the corresponding complex amplitudes $\tilde{\mathbf{U}} = [\tilde{U}_y, \tilde{\Theta}_z]^T$. \mathbf{F} is the corresponding vector of the external force F_y and moment M_z per unit length given as $\mathbf{F} = \tilde{\mathbf{F}} e^{i\omega t}$ in which $\tilde{\mathbf{F}}$ is the vector of the corresponding amplitudes $\tilde{\mathbf{F}} = [\tilde{F}_y, \tilde{M}_z]^T$.

By substituting Eq. (9) into the equations of motion, these are obtained in the wavenumber domain as:

$$((\mathbf{K}_p + \mathbf{K}_0 - \omega^2 \mathbf{M}) - i\xi \mathbf{K}_1 - \xi^2 \mathbf{K}_2) \tilde{\mathbf{U}} = \tilde{\mathbf{F}} \quad (10)$$

which can be written as:

$$\mathbf{A}(\xi, \omega) \tilde{\mathbf{U}} = \tilde{\mathbf{F}} \quad (11)$$

By extending this model and taking the sum of the stress resultants (forces and moments) acting on the centroid of an infinitesimal element in all three directions, instead of just the vertical direction, as well as the bi-moment in the axial direction due to warping [19], seven equations of motion for the fully coupled rail are obtained in matrix form similar to Eq. (3) and (10). \mathbf{U} becomes a vector of seven components of vibration (three displacements, three rotations and warping) at the centroid with the corresponding complex amplitudes:

$$\tilde{\mathbf{U}} = [\tilde{U}_x, \tilde{U}_y, \tilde{U}_z, \tilde{\Theta}_x, \tilde{\Theta}_y, \tilde{\Theta}_z, \tilde{U}_w]^T \quad (12)$$

Similarly, $\tilde{\mathbf{F}}$ will contain seven force components as:

$$\tilde{\mathbf{F}} = [\tilde{F}_x, \tilde{F}_y, \tilde{F}_z, \tilde{M}_x, \tilde{M}_y, \tilde{M}_z, \tilde{M}_w]^T \quad (13)$$

and the matrices \mathbf{K}_0 , \mathbf{K}_1 , \mathbf{K}_2 and \mathbf{M} for the fully coupled model are given by:

$$\mathbf{K}_0 = \begin{bmatrix} 0 & 0 & 0 & 0 & 0 & 0 & 0 \\ 0 & 0 & 0 & 0 & 0 & 0 & 0 \\ 0 & 0 & 0 & 0 & 0 & 0 & 0 \\ 0 & 0 & 0 & 0 & 0 & 0 & 0 \\ 0 & 0 & 0 & 0 & G A \kappa_z & 0 & G A \kappa_z e_y \\ 0 & 0 & 0 & 0 & 0 & G A \kappa_y & G A \kappa_y e_z \\ 0 & 0 & 0 & 0 & G A \kappa_z e_y & G A \kappa_y e_z & G J_t \end{bmatrix} \quad (14)$$

$$\mathbf{K}_1 = \begin{bmatrix} 0 & 0 & 0 & 0 & 0 & 0 & 0 \\ 0 & 0 & 0 & 0 & 0 & G A \kappa_y & G A \kappa_y e_z \\ 0 & 0 & 0 & 0 & -G A \kappa_z & 0 & -G A \kappa_z e_y \\ 0 & 0 & 0 & 0 & -G A \kappa_z e_y & -G A \kappa_y e_z & -G J_t \\ 0 & 0 & G A \kappa_z & G A \kappa_z e_y & 0 & 0 & 0 \\ 0 & -G A \kappa_y & 0 & G A \kappa_y e_z & 0 & 0 & 0 \\ 0 & -G A \kappa_y e_z & G A \kappa_z e_y & G J_t & 0 & 0 & 0 \end{bmatrix} \quad (15)$$

$$\mathbf{K}_2 = \begin{bmatrix} -EA & 0 & 0 & 0 & 0 & 0 & 0 \\ 0 & -G A \kappa_y & 0 & G A \kappa_y e_z & 0 & 0 & 0 \\ 0 & 0 & -G A \kappa_z & -G A \kappa_z e_y & 0 & 0 & 0 \\ 0 & G A \kappa_y e_z & -G A \kappa_z e_y & -G(J_t + J) & 0 & 0 & 0 \\ 0 & 0 & 0 & 0 & -EI_y & EI_{yz} & -EI_{wy} \\ 0 & 0 & 0 & 0 & EI_{yz} & -EI_z & EI_{wz} \\ 0 & 0 & 0 & 0 & -EI_{wy} & EI_{wz} & -EI_w \end{bmatrix} \quad (16)$$

$$\mathbf{M} = \begin{bmatrix} m & 0 & 0 & 0 & 0 & 0 & 0 \\ 0 & m & 0 & 0 & 0 & 0 & 0 \\ 0 & 0 & m & 0 & 0 & 0 & 0 \\ 0 & 0 & 0 & \rho I_p & 0 & 0 & 0 \\ 0 & 0 & 0 & 0 & \rho(I_y - I_{wy}) & -\rho I_{yz} & \rho I_{wy} \\ 0 & 0 & 0 & 0 & -\rho I_{yz} & \rho(I_z + I_{wz}) & -\rho I_{wz} \\ 0 & 0 & 0 & 0 & \rho I_{wy} & -\rho I_{wz} & \rho I_w \end{bmatrix} \quad (17)$$

in which

$$J_t = J_{rs} + A \kappa_y e_z^2 + A \kappa_z e_y^2$$

J_t is the secondary torsional constant, representing the effective shear area due to restrained warping shear stresses (i.e. J_{rs}) including the effects of eccentricity in the y and z axes. The effective shear area is given as [21]:

$$J_{rs} = \kappa_s (I_p - J) \quad (18)$$

where κ_s is a correction factor for the effective shear due to restrained torsional warping. As noted by Mokos and Sapountzakis [22], for open cross-sections (e.g. I-beams) the secondary torsional moment has only a small influence on the torsional behaviour of the beam, however, its inclusion leads to more accurate results. Thus the value of the correction factor κ_s will not influence the response of the beam significantly. Here, $\kappa_s = 1$ is used, similar to Sapountzakis and Tsipiras [21] and Gendy and Saleeb [23]. The support stiffness matrix \mathbf{K}_p is given below. The matrices \mathbf{K}_0 , \mathbf{K}_1 and \mathbf{K}_2 contain the same information as those presented by Kim et al. [19] for the force-deformation equations of a static beam column, while matrix \mathbf{M} accounts for the inertial effects.

The coupling terms that are included in the model are found in off-diagonal terms of the above matrices. For example, off-diagonal terms containing EI_{yz} represent coupling between vertical and lateral bending. Similarly, the following terms are seen for coupling with the respective degrees of freedom: e_y and e_z for the effect of shear-centre eccentricity in coupling bending and torsion, EI_{wy} and EI_{wz} for coupling with warping behaviour in the respective direction and finally GA_t for the coupling of warping with torsion.

Finally, the model presented by Kim et al. [19] has been extended to include an elastic support, representing the rail pad usually located beneath the rail foot. The stiffness matrix of the support is given by \mathbf{K}_p which includes the effect of the distances y_f and z_f between the rail centroid and the centre of the upper surface of the rail pad (here $z_f = 0$). This matrix can be given as:

$$\mathbf{K}_p = \mathbf{T}_f^T \mathbf{K}_{p,f} \mathbf{T}_f \quad (19)$$

where

$$\mathbf{K}_{p,f} = \text{diag}(k_x, k_y, k_z, k_{xr}, k_{yr}, k_{zr}, k_w) \quad (20)$$

contains the stiffnesses in each direction, and

$$\mathbf{T}_f = \begin{bmatrix} 1 & 0 & 0 & 0 & z_f & -y_f & \phi_f \\ 0 & 1 & 0 & -z_f & 0 & 0 & 0 \\ 0 & 0 & 1 & y_f & 0 & 0 & 0 \\ 0 & 0 & 0 & 1 & 0 & 0 & 0 \\ 0 & 0 & 0 & 0 & 1 & 0 & 0 \\ 0 & 0 & 0 & 0 & 0 & 1 & 0 \\ 0 & 0 & 0 & 0 & 0 & 0 & 1 \end{bmatrix} \quad (21)$$

is a transformation matrix, where $\phi_f(y, z)$ is the warping function of the cross-section. The

translational stiffnesses per unit length are derived from the stiffness per pad (e.g. k_y^p), similar to the Timoshenko beam model in vertical bending. For simplicity the rotational stiffnesses are estimated from the translational stiffnesses per pad, assuming a homogeneous material for the pad [24], as:

$$k_{xr}^p = k_{zr}^p = \frac{l_p^2}{12} k_y^p \quad (22)$$

in which it is assumed that the pad is square with length l_p . Excellent agreement was found by Thompson et al. [24] between values calculated using the above equation and those measured directly, with an average difference of 1%. Similarly, k_{yr}^p is given by:

$$k_{yr}^p = \frac{l_p^2}{12} k_x^p + \frac{l_p^2}{12} k_z^p \quad (23)$$

in which it can be assumed that the pad stiffnesses in the axial and lateral direction are identical (i.e. $k_z^p = k_x^p$). As for the translational stiffnesses these are converted into a stiffness per unit length (e.g. $k_{yr} = k_{yr}^p/l_{sl}$). The foundation resistance to warping k_w is similarly defined as:

$$k_w^p = (\kappa_w e_s)^2 \frac{l_p^2}{12} k_x^p \quad (24)$$

where κ_w is a factor relating the axial deformation of the railfoot due to warping to the warping amplitude (assuming a linear profile) and e_s is the vertical distance between the rail foot and the rail shear centre ($y_f - e_y$).

2.2. Finite Element model

In order to validate the developed model, a comparison is made with results from a finite element model obtained using the COMSOL Multiphysics [25] Finite Element package. The comparison is made in terms of the dispersion relationship of a free rail only. Different waves propagate at different frequencies and the wavenumber represents the phase change per unit length. The dispersion plot is the wavenumber plotted against frequency, which allows identification of the propagating waves at each frequency. Also the individual wavespeeds can be obtained through the relationship ω/ξ .

Firstly the geometry of the rail (60E1) was introduced in COMSOL and the geometric properties were derived to be used in the theoretical model for the comparison (Table 1). Then a 3D model with a length of 1.2 m was created and a modal analysis was performed in order to find the eigen-frequencies and the mode shapes of the system. This was done for three different boundary conditions at the ends of the rail section, namely symmetric-symmetric, antisymmetric-symmetric and antisymmetric-antisymmetric.

After obtaining the eigen-frequencies of the system, and by observing the mode shapes, the wavenumber can be obtained according to the boundary conditions (see Ryue et al. [13]). The modes have a sinusoidal modeshape in the axial direction. For symmetric-symmetric

(or antisymmetric-antisymmetric) conditions, the wavenumber is obtained as $n\pi/L$ where L is the length of the rail section modelled in COMSOL and n is an integer indicating the number of half-waves within the length. Similarly for antisymmetric-symmetric conditions, the wavenumber is obtained as $(2n + 1)\pi/2L$ where n is an integer.

One of the limitations of using the Finite Element approach to obtain the dispersion relationship, is that a fine resolution, especially at low frequency in terms of a logarithmic scale, can only be achieved by a very long section of rail. This is due to the fact that the wavenumber is inversely proportional to the length of the the model. Thus, the WFE method is also employed.

2.3. Waveguide Finite Element model

In order to validate the model, a waveguide finite element (WFE) model based on that presented by Nilsson et al. [14] has been utilised to obtain the dispersion relations for a free and supported rail (where $\mathbf{K}_p = \mathbf{0}$ for a free rail). This model uses the same form of equations of motion in matrix form as in Eq. (3) although with much larger matrices to account for all the nodal degrees of freedom. The rail is represented here by 32 eight-noded quadrilateral elements, as shown in Fig. 2, and the support by spring elements under each node at the base of the rail foot. The model has 423 degrees of freedom.

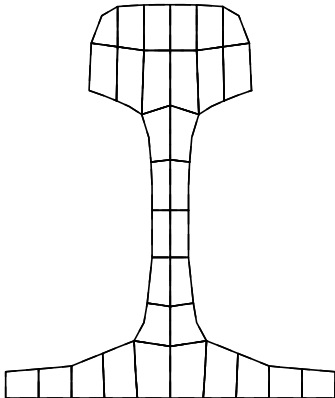


Figure 2: Mesh of 60E1 rail in the WFE model

In terms of computational time, on a personal computer the WFE model required just over an hour to perform the calculation for the dispersion relationship and mobility over 1200 frequency steps, while the semi-analytical model presented here required 12 seconds.

2.4. Dispersion relation

In order to obtain the dispersion relation, the free vibration of the rail ($\tilde{\mathbf{F}} = \mathbf{0}$) is considered. For such a case, non-trivial solutions require $|\mathbf{A}| = 0$. This is a dual (non-linear) eigenvalue problem in ξ and ω . In order to simplify the solution process, the 7×7 non-linear eigenvalue problem is rewritten as an equivalent 14×14 linear eigenvalue problem [26]. This is achieved by re-writing Eq. (11) in the form:

$$\mathbf{A}_1 \mathbf{v} + i\xi \mathbf{A}_2 \mathbf{v} = \mathbf{0} \quad (25)$$

where

$$\mathbf{A}_1 = \begin{bmatrix} \mathbf{K}_0 - \omega^2 \mathbf{M} & -\mathbf{K}_1 \\ \mathbf{0}_{7 \times 7} & \mathbf{I}_{7 \times 7} \end{bmatrix} \quad (26)$$

$$\mathbf{A}_2 = \begin{bmatrix} \mathbf{0}_{7 \times 7} & \mathbf{K}_2 \\ -\mathbf{I}_{7 \times 7} & \mathbf{0}_{7 \times 7} \end{bmatrix} \quad (27)$$

and $\mathbf{v} = \{\tilde{\mathbf{U}}, i\xi\tilde{\mathbf{U}}\}^T$.

The above system of equations can be solved as an eigenvalue problem for $\lambda = -i\xi$, i.e. $\mathbf{A}_1 \mathbf{v} = \lambda \mathbf{A}_2 \mathbf{v}$, yielding 14 solutions for $\xi(\omega) = i\lambda$. Due to the forms of the various matrices, these solutions can be divided into two sets with $\text{Im}(\xi) \leq 0$ propagating in the positive direction and $\text{Im}(\xi) \geq 0$ propagating in the negative direction, with the second set given by $\xi_2 = -\xi_1$. When damping is included there are no solutions with $\text{Im}(\xi) = 0$.

The section properties of 60E1 rail (see Figure 1) have been determined using the finite element software COMSOL and are listed along with the assumed material properties in Table 1.

Table 1: Rail section properties (inertial properties relative to centroid)

Parameter	Value	Units
Young's modulus, E	210	GPa
Shear modulus, G	80.769	GPa
Density, ρ	7860	kg/m ³
Poisson's ratio, ν	0.3	-
Cross-section area, A	7.670×10^{-3}	m ²
Second moment of area about y -axis, I_y	512.7×10^{-8}	m ⁴
Second moment of area about z -axis, I_z	3037×10^{-8}	m ⁴
Product moment of area, I_{yz}	0	m ⁴
Polar moment of area, I_p	3.550×10^{-5}	m ⁴
Torsional constant, J	2.212×10^{-6}	m ⁴
Vertical shear coefficient, κ_y	0.393	-
Lateral shear coefficient, κ_z	0.538	-
Vertical shear centre eccentricity, e_y	0.033	m
Lateral shear centre eccentricity, e_z	0	m
Warping constant, I_w	2.161×10^{-8}	m ⁶
Warping product moment of area, I_{wy}	1.6971×10^{-7}	m ⁵
Warping product moment of area, I_{wz}	0	m ⁵
Warping factor for rail foot, k_w	-0.6016	-

Figure 3 shows the dispersion relationship for an unsupported 60E1 rail obtained from both the present beam model (solid lines) and the FE model (markers). Similarly, Fig. 4(a) shows the dispersion relationship for an unsupported 60E1 rail obtained from the present beam model (solid lines) and the WFE model (dots). There are virtually no differences

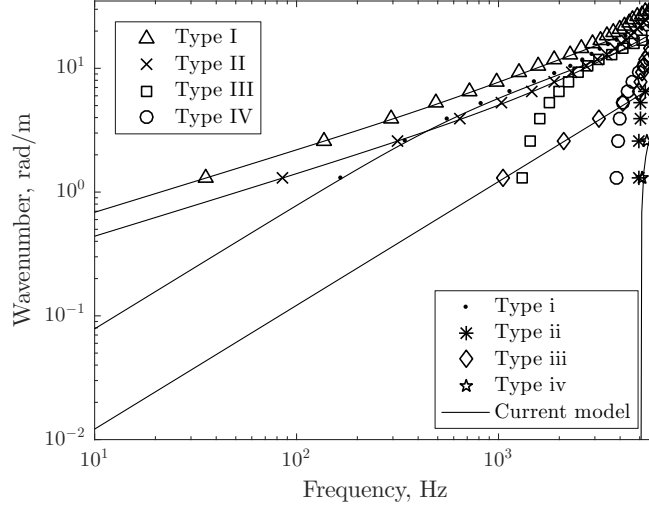


Figure 3: comparison of dispersion curves for a free 60E1 rail with those from the FE model

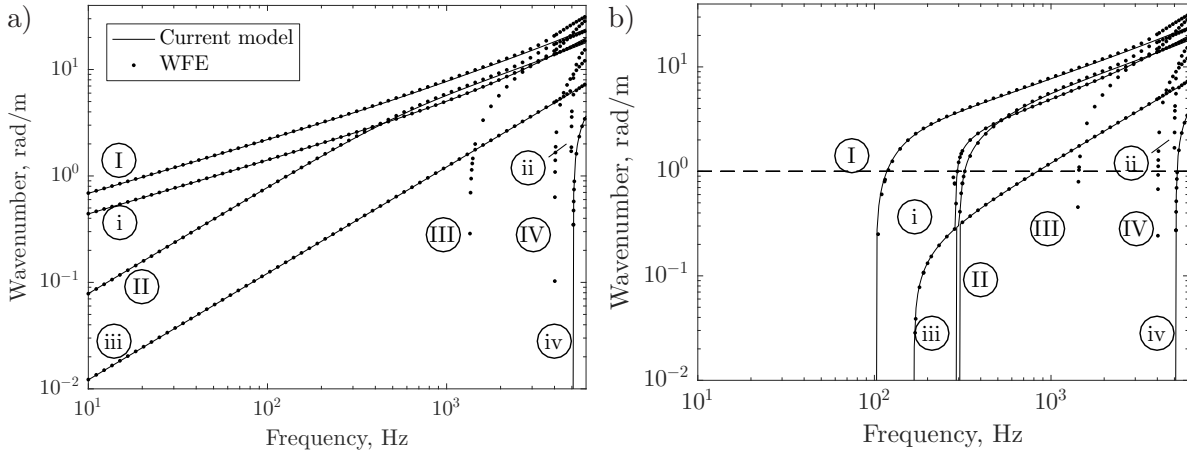


Figure 4: Comparison of dispersion curves for a 60E1 rail with those from the WFE model for a (a) free and a (b) supported rail.

between the results of the FE and WFE models. In both figures, each wave is identified by a Roman numeral, with lower case letters for vertical/longitudinal waves and upper case for lateral waves [20, 27]. Due to symmetry of the rail section, it is found that the lateral and vertical/longitudinal waves are uncoupled from each other as their dispersion curves cross without veering [28, 29].

The vertical motion includes two main wave-types. The first is the vertical bending (type i) which is well predicted by the present beam model, while the second is a higher-order wave associated with the foot flapping (type ii) which cuts on at about 5 kHz and is not represented by the present beam model. Longitudinal waves include the first order axial wave (type iii) and a higher order axial wave (type iv) both of which are well predicted by the present beam model. The first two lateral wave types correspond to lateral bending (type I) and torsion

(type II) which are well represented, at least up to 1 kHz. Two higher-order waves appear at higher frequencies, corresponding to the bending (type III) and double bending (type IV) of the web. These cut on at about 1.3 and 4 kHz in the WFE model but are not predicted by the current beam model, because the cross-section deformation is not included in the present model (i.e. no separation of head, web and flange). This also means that the lateral bending wave, for example, above 3 kHz does not match exactly that of the WFE model since in the latter case it is influenced by the cross-section deformation. The added flexibility in the web in the WFE model causes waves to travel at higher wavenumbers. Similarly, the torsional wave (lateral wave type II) is seen to be influenced by the web bending in the WFE model at higher frequencies.

Table 2: Properties of track support.

Parameter	Value
Railpad axial stiffness, k_x^p	40 MN/m
Railpad vertical stiffness, k_y^p	120 MN/m
Railpad lateral stiffness, k_z^p	40 MN/m
Rail foot warping factor, κ_w	-0.601
Pad loss factor, η_p	0.25
Railpad width (rail foot), l_p	150 mm
Foot to centroid distance, y_f	81 mm
Foot to centroid distance, z_f	0 mm
Sleeper spacing, l_{sp}	0.65 m

Figure 4(b) similarly shows the dispersion relationship for a 60E1 rail on a continuous undamped support with the parameters listed in Table 2. In comparison with Figure 4(a), the influence of the support is mainly seen at frequencies below 400 Hz, where the wavenumbers of the first vertical bending wave (type i), the first-order longitudinal wave (type iii) and the lateral bending and torsion waves (types I & II) now have non-zero cut-on frequencies. These frequencies are identified for the supported rail as 290.0 Hz, 168.0 Hz, 102.8 Hz and 302.3 Hz respectively. The first two frequencies can be found approximately from the formulae $f_{co,v} = \sqrt{k_y/m}/2\pi \approx 289.9$ Hz and $f_{co,a} = \sqrt{k_x/m}/2\pi \approx 167.4$ Hz. Due to the vertical offset of the foundation from the centroid, the cut-on frequencies for the two lateral waves do not correspond to the equivalent formulae $f_{co,l} = \sqrt{k_z/m}/2\pi \approx 167.4$ Hz and $f_{co,t} = \sqrt{k_{xr}/\rho I_p}/2\pi \approx 184.5$ Hz. Instead the eccentricity causes the first cut-on frequency to reduce and the second to increase. The cut-on frequencies of the higher order waves are primarily influenced by the cross-sectional properties and thus remain unaffected by the support properties. The corresponding mode shapes obtained from the WFE model for all the above identified waves are presented in Fig. 5, at a wavenumber near to 1 rad/m (shown by the dashed line in Fig. 4(b)).

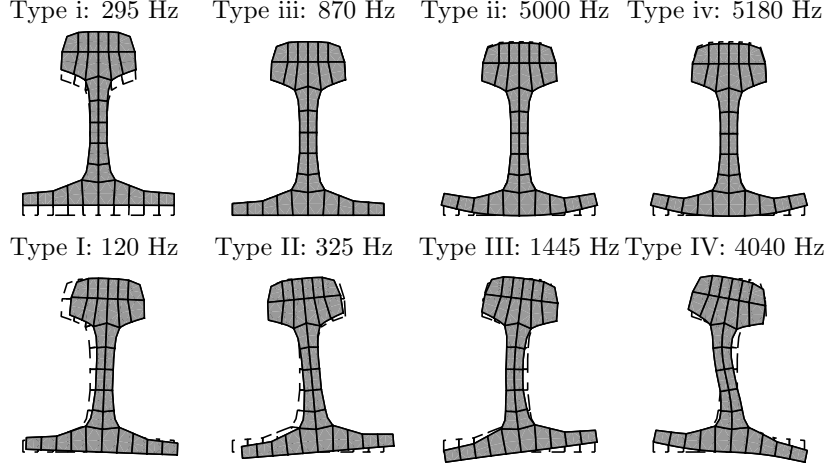


Figure 5: Examples of wave modes of 60E1 rail obtained from WFE model at a wavenumber of 1 rad/m

3. Mobility and decay rates

In this section the forced response is considered in terms of the point mobility in both vertical and lateral directions. This is again compared with results obtained using the WFE model as well as those obtained using the classical Timoshenko beam model. The results are calculated for the same track properties as before, with the only difference being that a damping loss factor is introduced for the rail ($\eta_r = 0.02$) making the corresponding Young's modulus complex with the form $E(1+i\eta_r)$. Similarly, a damping loss factor is also introduced for railpads ($\eta_p = 0.25$ in each direction), making again the corresponding stiffnesses complex with the form $k(1+i\eta_p)$.

3.1. Closed form solution for the response

For a given frequency and wavenumber, Eq. (11) can be solved for the complex amplitudes, to give:

$$\tilde{\mathbf{U}} = \mathbf{A}^{-1}\tilde{\mathbf{F}} \quad (28)$$

In order to find the response in the spatial domain, the inverse Fourier transform is required:

$$\mathbf{U}(x) = \frac{1}{2\pi} \int_{-\infty}^{\infty} \mathbf{A}^{-1}\tilde{\mathbf{F}}e^{-i\xi x} d\xi \quad (29)$$

The above integration can be performed either numerically or analytically. Here, the latter is preferred, using the contour integration method from the theory of complex variables [30].

The integration of a function ($f(\xi)e^{-i\xi x}$) along the real axis from $\xi_a \rightarrow -\infty$ to $\xi_b \rightarrow \infty$, is equivalent to the closed path integration along the real axis from ξ_a to ξ_b plus the integration along the lower semicircle from ξ_b to ξ_a , provided that the integration along the semicircle

is zero. This is satisfied for $x \geq 0$, while for $x \leq 0$ the upper semicircle needs to be used instead.

Then the residue theorem is utilised, with the solution in the spatial domain given for $x \geq 0$ as (see also Nilsson et al. [14]):

$$\mathbf{U} = -i \sum_{n=1}^N \frac{\mathbf{U}_{\mathbf{nL}} \tilde{\mathbf{F}}}{\mathbf{U}_{\mathbf{nL}} \mathbf{A}'(\xi_n) \mathbf{U}_{\mathbf{nR}}} \mathbf{U}_{\mathbf{nR}} e^{-i\xi_n x} \quad (30)$$

where $\mathbf{U}_{\mathbf{nL}}$ and $\mathbf{U}_{\mathbf{nR}}$ are the left and right eigenvectors of the eigenvalue problem in Eq. (11), the dash (') means the derivative with respect to ξ and ξ_n are the N eigenvalues on the lower half-plane with $\text{Im}(\xi_n) < 0$. From Eq. (10) the derivative can be written as:

$$\mathbf{A}'(\xi_n) = -i\mathbf{K}_1 - 2\xi_n \mathbf{K}_2 \quad (31)$$

Finally, if the force vector is set to unity in one direction and zero in the others, the mobility can be calculated as:

$$\mathbf{V} = \frac{\partial \mathbf{U}}{\partial t} = i\omega \mathbf{U} \quad (32)$$

3.2. Point mobility

Figure 6 shows the mobility of the 60E1 rail excited at various positions. Three different results are shown here, in each case: from the current semi-analytical beam model presented above, the WFE model and the classical analytical Timoshenko beam model for comparison. Figures 6(a) and 6(b) show the vertical and lateral mobility, excited at positions 1 and 2 respectively from Fig. 1. Two additional locations have also been selected, which are 20 mm from the web centreline for the vertical excitation (position 4) and at the top of the rail head for the lateral excitation (position 1 but force applied laterally). These results are shown in Figs 6(c) and 6(d) respectively.

For the vertical direction, Fig. 6(a), the current beam model shows excellent agreement with the WFE model for frequencies up to about 4 kHz. Above this frequency, cross-sectional deformation starts to become important and to influence the response of the rail. Two peaks occur in Fig. 6(a). The first occurs at the cut-on frequency of the vertical bending wave, $f_{co,v}$ at about 290 Hz. The second is seen for the WFE model only, at about 5 kHz. This corresponds to the cut-on frequency of the higher order vertical wave (type ii - foot flapping) see Fig. 4(b), which is not present for the current beam models. Comparing the developed beam model with the Timoshenko one, no differences are seen in the vertical mobility at the centre of the railhead.

For the lateral direction, Fig. 6(b), the agreement between the current beam model and the WFE model is again good at all frequencies. Two peaks can be identified at low frequencies, one at about 100 Hz, corresponding to the cut-on of wave type I and the other at about 300 Hz corresponding to wave type II. A third peak is seen in the results from the WFE model at about 1.4 kHz, corresponding to the cut-on frequency of the higher order lateral wave (type III - web bending). The average difference between the beam and

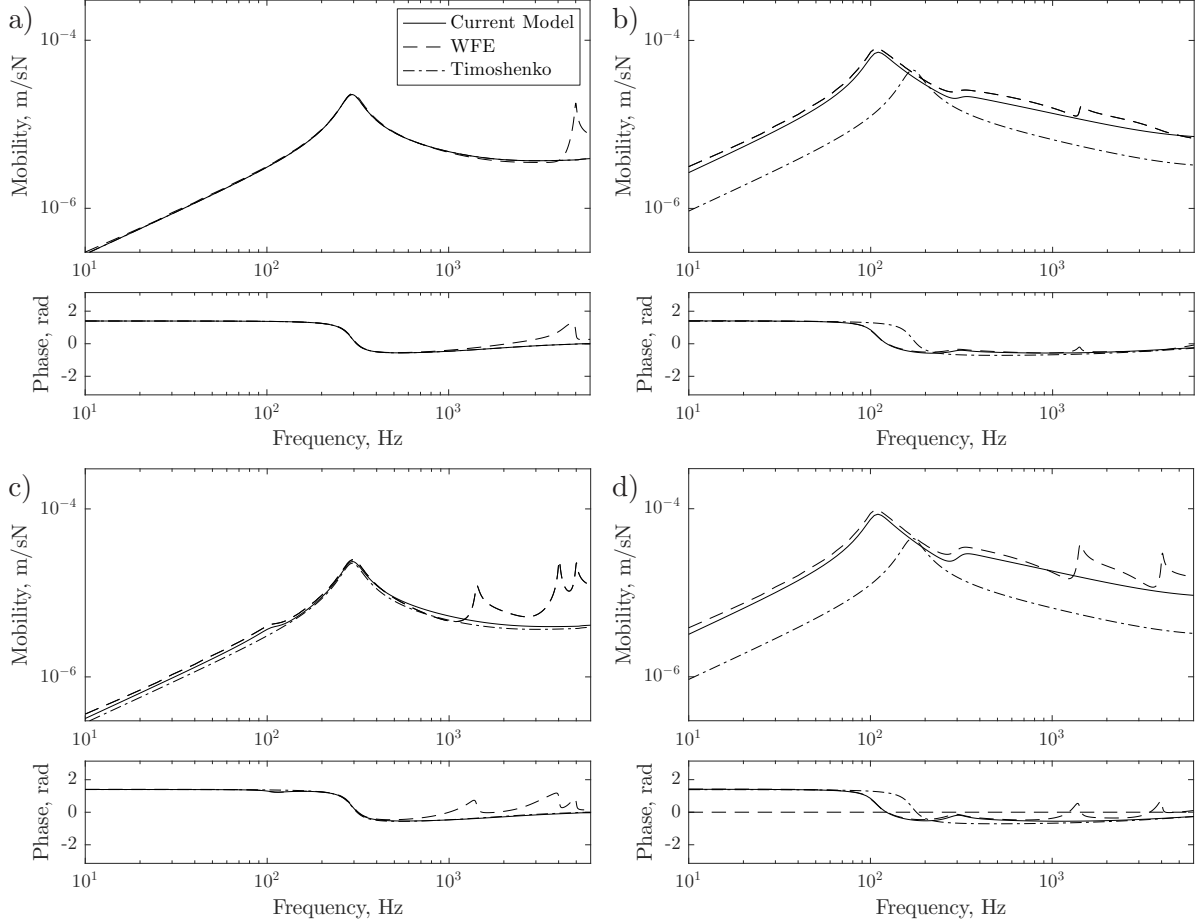


Figure 6: Point mobility for 60E1 rail (a) Vertical at Pos. 1; (b) Lateral at Pos. 2; (c) Vertical at Pos. 4; (d) Lateral at Pos. 1

WFE models is 14%. Significant differences are seen in the mobility relative to the classical Timoshenko beam model, which is on average a factor of 2 smaller. The cut-on frequency for the first lateral wave is seen in the Timoshenko beam model at $f_{co,l} = 167.4$ Hz, while that of the second lateral wave is not present as torsion is neglected. The differences between the analytical and semi-analytical models are caused by two main effects. The first is related to the foundation eccentricity. This causes the cut-on frequency of the lateral wave type I to reduce, thus shifting the peak in the mobility from 167.4 Hz to 102.8 Hz. The second is related to the inclusion of torsion in the beam model, since the rail is excited with an offset from the shear centre. Without torsion, the mobility is significantly lower over the whole frequency range. Even if the cut-on frequency of the wave type I for the Timoshenko beam in lateral bending is adjusted to 102.8 Hz (by setting $k_z^p = 15.2$ MN/m), the average difference between the models remains the same.

Figure 6(c) shows the results when an eccentric load is considered in the vertical direction. Apart from the peaks at the two vertical wave cut-on frequencies, three additional peaks are

seen in the results from the WFE model, corresponding to the cut-on of lateral waves at 100 Hz, 1.4 kHz and 4 kHz (see Fig. 4(b)). Of these, only the first is seen in the results from the semi-analytical model. At all frequencies, the mobility of the beam model is higher than for the Timoshenko beam, with an average difference of 10%.

The results in Fig. 6(d) indicate that, seen at the top of the rail head, the lateral mobility is higher than at the centre of the rail head. At high frequencies the higher order lateral waves lead to an increase in the mobility by 60% on average above 1.4 kHz, compared with the centre of the rail head (see also [9]). At lower frequencies the difference remains at about 10%.

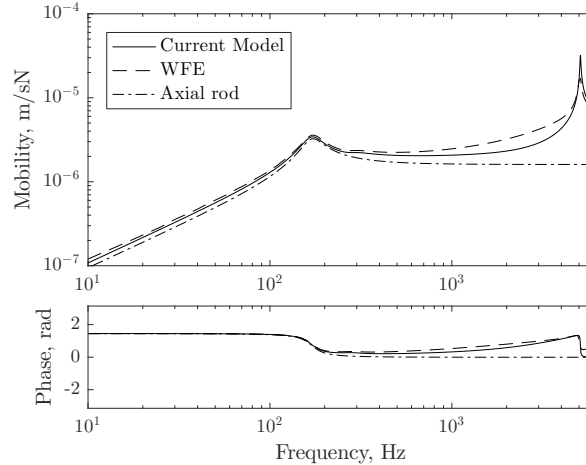


Figure 7: Axial point mobility for 60E1 rail excited at position 1

Figure 7 shows the axial mobility of the rail when excited at position 1 from Fig. 1. For comparison, an axial rod model is also shown. For all three models, a peak is seen at about 170 Hz, corresponding to the cut-on of the first-order longitudinal wave (type iii), as seen from Fig. 4(b). A further distinct peak is seen in the WFE and current model at about 5 kHz, corresponding to the cut-on of wave type iv. The agreement is good over the whole frequency range presented.

Figures 8 (a) and (b) depict the lateral mobility at position 2 due to a vertical force (cross mobility) for an offset of 10 mm and 20 mm (positions 3 and 4 respectively of Fig. 1). The cross mobility for the Timoshenko beam model is based on the geometrical average of the vertical (A_y) and lateral (A_z) receptances as [4]:

$$A_{yz} = 10^{XdB/20} \sqrt{A_y A_z} \quad (33)$$

where $XdB = 20\log_{10}X$ is an empirical factor used in TWINS that is typically set around -10 dB. In order to obtain a suitable factor, calculations are performed with the Timoshenko beam model for a range of values and the one providing the best fit with the semi-analytical beam model was selected. This was -14 dB for an offset of 10 mm (Fig. 8(a)) and -8 dB for an offset of 20 mm (Fig. 8(b)). Additionally, in the Timoshenko beam model the lateral pad stiffness has been reduced to 15.2 MN/m to match the cut-on frequency of wave type I.

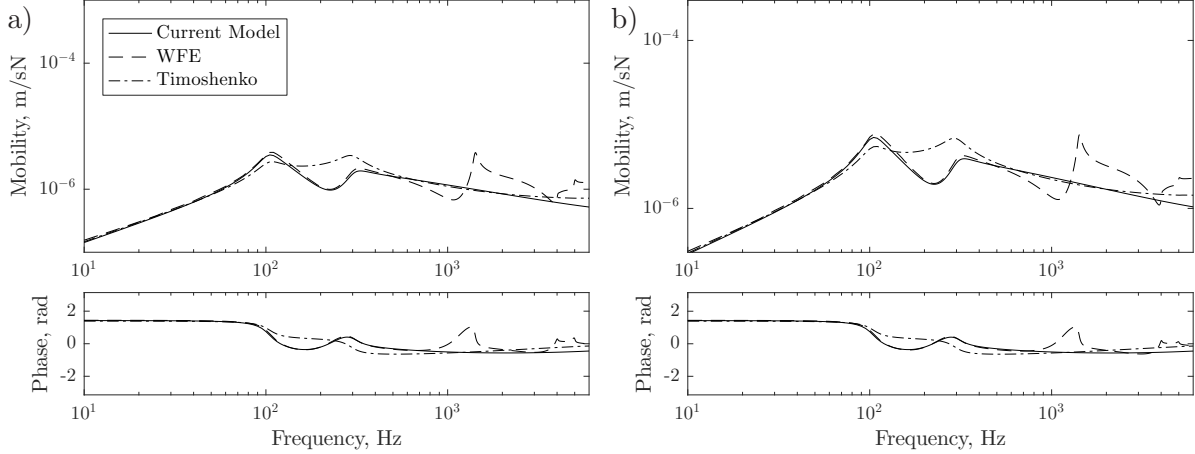


Figure 8: Cross mobility for 60E1 rail excited in the vertical direction (a) position 3 ($X_{dB} = -14$ dB); (b) position 4 ($X_{dB} = -8$ dB)

In both cases, the current beam model shows good agreement with the WFE model for frequencies up to about 1 kHz. Above this frequency, cross-sectional deformation, especially for an offset of 20 mm, starts to become important and to influence the response of the rail. The empirical relationship does not capture the drop in the mobility between 100 and 300 Hz but otherwise gives similar results to the present model. However it relies on the selection of the factor X_{dB} whereas the offset in the present model is a more intuitive physical quantity.

3.3. Decay rate and transfer mobilities

Here, results are presented for the track decay rate and transfer mobility along the rail, calculated from the forced response. Results for both vertical and lateral excitations are presented for a typical railway track, properties of which are listed in Table 2.

The track decay rate can be obtained by two different methods. The first is by considering the imaginary part of the damped wavenumbers from the dispersion relationship [9]. This results in a decay rate for each wave. The second is to calculate the total response at different positions along the rail (transfer mobility) and to obtain the decay rate according to the experimental method [31, 32], thus obtaining the decay rate accounting for the combined response due to all wave types.

The decay rates (in dB/m) for each wave are obtained using the relationship [9]:

$$\Delta_{pw} = 20 \log_{10} (e^{\text{Im}(\xi)}) = -8.686 \text{Im}(\xi) \quad (34)$$

These are shown in Figures 9(a,b) for the vertical and lateral waves. It is seen that the axial wave, type iii, has the lowest decay rate. As well as the various propagating waves, evanescent waves exist associated with bending (Ve and Le). These cut on as shear waves at high frequency in a Timoshenko beam model. For each of the propagating waves, types I, II, i and iii, the decay rate drops from an initially high value at around the cut-on frequency of the wave [20]. This also occurs for the higher order shear wave type Ve which becomes type

iv at around 5 kHz. Finally, the wave type w consists of a predominantly warping motion of the cross-section. This wave has a high decay rate and is thus not expected to influence the response significantly away from the excitation point.

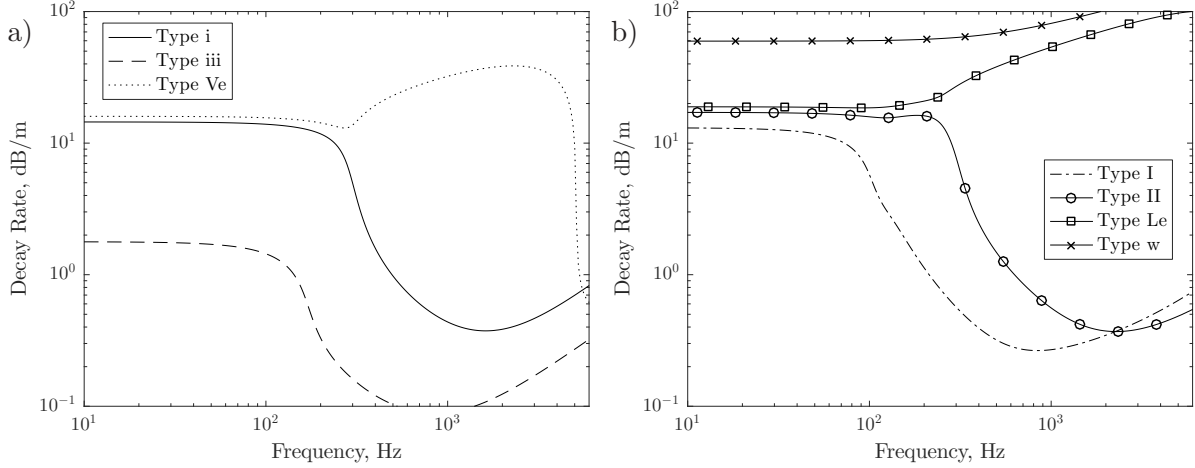


Figure 9: Decay rates for each wave obtained from semi-analytical model (a) vertical waves; (b) lateral waves

The overall decay rate in each one-third octave band is evaluated from predicted transfer mobilities according to the standard measurement method as [31]:

$$\Delta = \frac{4.343}{\sum_{x=0}^{x_{max}} \frac{|A(x_n)|^2}{|A(x_0)|^2} \delta x_n} \quad (35)$$

where $A(x_n)$ is the calculated mobility at a distance x_n away from the excitation point, $A(x_0)$ is the mobility at the excitation point and δx_n is the length of rail segment associated with the point x_n . The calculation is carried out in one-third octave frequency bands.

According to the standard [31], the vertical response of the rail should be obtained using excitation at the middle of the rail head. Since this excitation would not result in any differences due to coupling sources in the rail (see Fig. 6(a)), a different location is used here for illustrative purposes. Thus, to calculate the vertical response, the rail is excited at position 4, 20 mm from the centre of the railhead, and the response is obtained at the same position at various distances x_n . The decay rate for vertical excitation is plotted in Fig. 10(a), while the corresponding point mobility can be seen in Fig. 6(c). Equivalently, results for the lateral track decay rate are shown in Fig. 10(b), where the force and response points are located at position 2, 20 mm below the top of the railhead, with the corresponding mobility seen in Fig. 6(b).

At low frequencies, the vertical decay rates are high due to the blocking effect of the support, similar to the result for the vertical wave alone. They drop at around the cut-on frequency of the rail vertical bending wave ($f_{co,i}$). At high frequencies, the decay rate increases due to damping in the rail [32]. Similar behaviour is observed for the lateral direc-

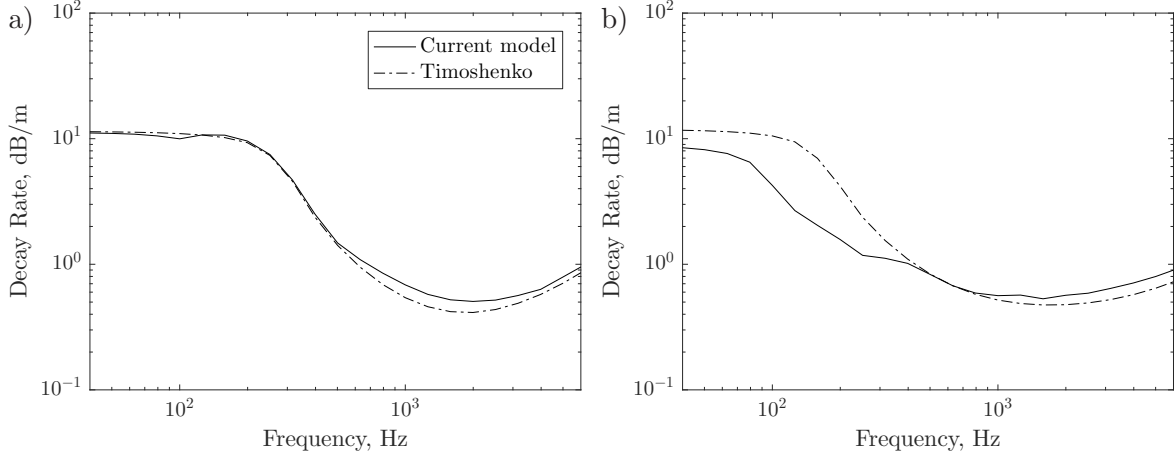


Figure 10: Track decay rate obtained using current semi-analytical model and analytical Timoshenko beam model for (a) vertical and (b) lateral excitation

tion, with the decay rate dropping at a lower frequency ($f_{co,I}$) due to the smaller foundation stiffness associated with this direction.

Results are also shown in Fig. 10 for the Timoshenko beam model. For the vertical case, differences between the models occur mainly due to the eccentric applied load which excites the type I and II lateral waves as well as the vertical waves. Above 400 Hz, the vertical decay rate of the current model becomes higher than the conventional Timoshenko model, due to the higher decay rate of the lateral wave type II. If the rail is excited through its centreline both curves would be identical.

The most significant difference is seen in the lateral track decay rate, where the result is lower than that of the Timoshenko model for frequencies below 300 Hz. This is caused by the lowering of the cut-on frequency for the lateral wave type I. Consequently, if the track decay rate is used for parameter fitting from measurements, using the Timoshenko beam model will lead to a significantly different estimate of the lateral pad stiffness. Above 300 Hz, the decay rate is higher than for the Timoshenko model.

The contribution of the individual waves to the overall mobility at different distances is shown in Fig. 11 for example frequencies. For the vertical response, at 50 Hz all waves have a relatively high decay rate, with the lateral wave I having the lowest (apart from the axial wave). Thus, at a distance away from the excitation, the response is seen to be influenced most by this lateral wave. As this first lateral wave cuts on at 100 Hz, by 150 Hz the response is strongly influenced by it. Above the cut-on frequency of the vertical bending wave (290 Hz), the vertical wave dominates the response.

When the rail is excited laterally, the vertical and axial degrees of freedom are not excited. The lateral mobility is mainly influenced by the lateral wave I for the frequencies considered, as this has the lowest decay rate. As the second lateral wave cuts on at 302 Hz, its mobility starts to increase in Fig. 11(f), but it still has a smaller amplitude than the first lateral wave. Oscillations occur due to interference between these two waves.

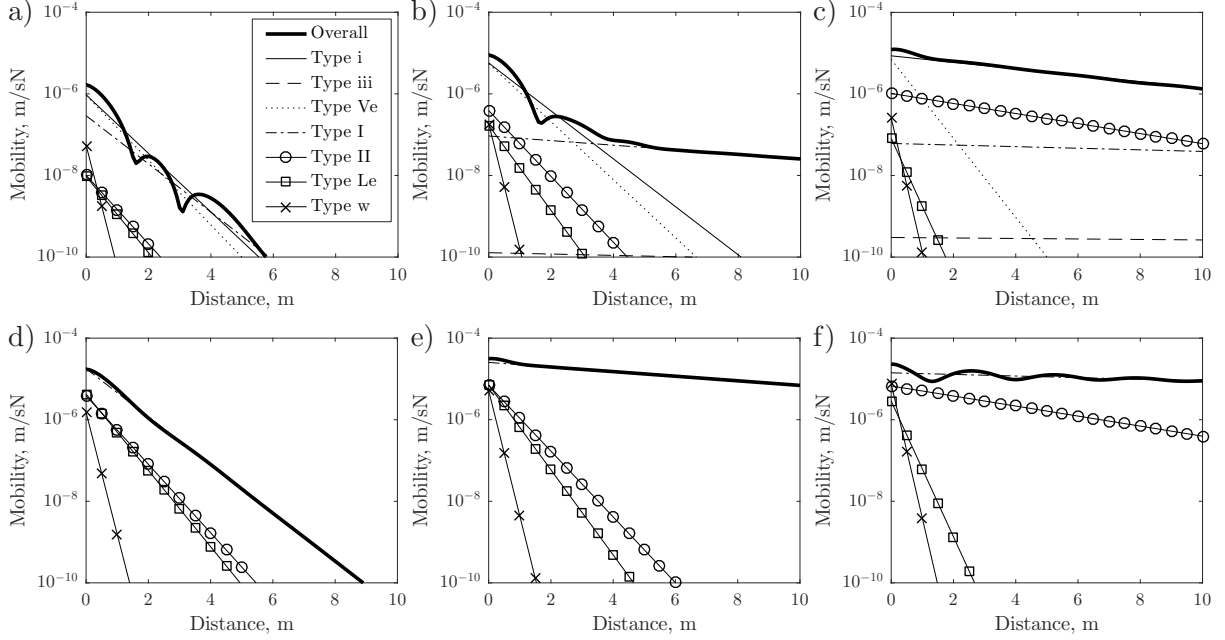


Figure 11: Vertical and lateral transfer mobility per wave and overall (a) Vertical at 50 Hz; (b) Vertical at 150 Hz; (c) Vertical at 300 Hz; (d) Lateral at 50 Hz; (e) Lateral at 150 Hz; (f) Lateral at 300 Hz

4. Comparison with measurements

Finally, a comparison is made between the model presented here and measurements performed on a 33 m long test track at the University of Southampton. Results are also shown for the Timoshenko beam model. The aim of these comparisons is two-fold: a) to compare the performance of the two models in extracting track parameters based on the point mobilities and track decay rates and b) to give additional validation of the model.

In order to represent the track in the models more accurately, a two-layer support has been introduced [20], representing the sleepers as a mass layer and the ballast as a layer of damped springs. Because the track properties are not fully known, a basic curve fitting procedure based on the track decay rate is performed in order to aid the determination of the pad and ballast stiffness and damping, while maintaining the same rail and sleeper properties. Table 3 shows the derived parameters.

The point mobilities and track decay rates for vertical and lateral excitation are plotted in Figs 12 and 13 respectively. The measured point mobility, when plotted in narrow frequency resolution, exhibits oscillations at frequencies above 600 Hz, attributed to reflections from the ends of the finite length of track. To suppress these, the results are presented here in one-third octave frequency bands.

The model shows a very good agreement with the measurements for both the mobility and decay rates up to 2000 Hz. The agreement for vertical excitation is slightly better than for the lateral direction. It is seen that the estimated lateral pad stiffness is significantly higher than when fitting with a simple Timoshenko beam model.

Table 3: Derived properties for test track.

Parameter	Current model	Timoshenko
Sleeper model	Bi-bloc	Bi-bloc
Sleeper mass (per rail), m_s^b	150 kg	150 kg
Sleeper spacing, l_{sp}	0.63 m	0.63 m
Rail loss factor, η_r	0.01	0.01
Pad axial stiffness, k_x^p	100 MN/m	35 MN/m
Pad vertical stiffness, k_y^p	120 MN/m	120 MN/m
Pad lateral stiffness, k_z^p	100 MN/m	35 MN/m
Pad vertical loss factor, $\eta_{p,v}$	0.25	0.25
Pad lateral loss factor, $\eta_{p,l}$	0.2	0.2
Ballast axial stiffness, $k_{x,b}$	100 MN/m	100 MN/m
Ballast vertical stiffness, $k_{y,b}$	100 MN/m	100 MN/m
Ballast lateral stiffness, $k_{z,b}$	100 MN/m	100 MN/m
Ballast vertical loss factor, $\eta_{b,v}$	0.5	0.5
Ballast lateral loss factor, $\eta_{b,l}$	1	1

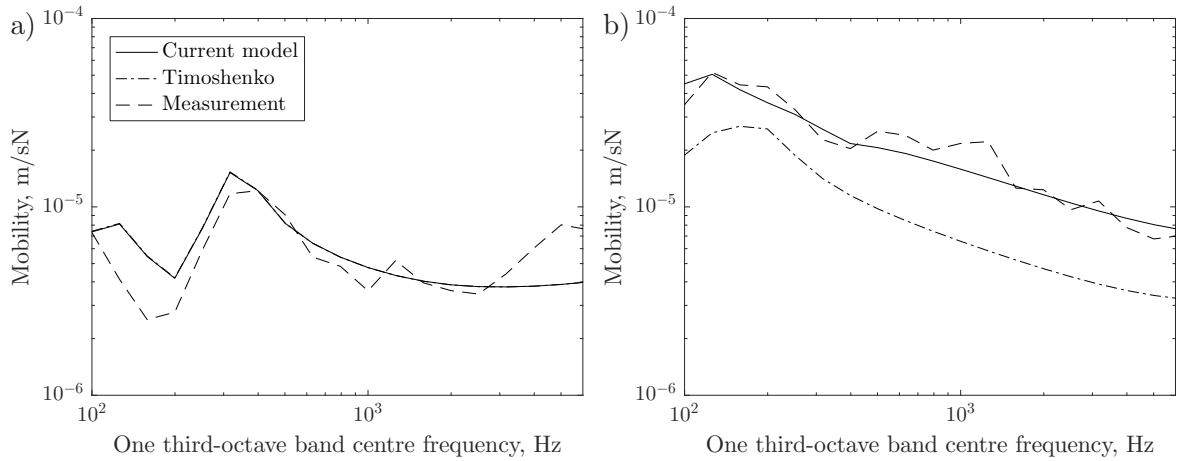


Figure 12: Point mobility comparison against measurements for test track (a) vertical; (b) lateral

As seen from Fig. 12(b), a significant improvement is obtained in the lateral mobility using the proposed model, compared with the Timoshenko beam model. The main reason for this, as shown in previous sections, is the inclusion of torsion in the model. What is important from this figure is the fact that, even though the model does not include cross-sectional deformation, the main trend in the lateral mobility is adequately represented over the whole frequency range.

In Fig. 13, the overall comparison with the measured track decay rate is satisfactory for frequencies up to about 2 kHz. Above that frequency, the measured track decay rate increases significantly, for both the vertical and lateral directions due to cross-sectional deformations.

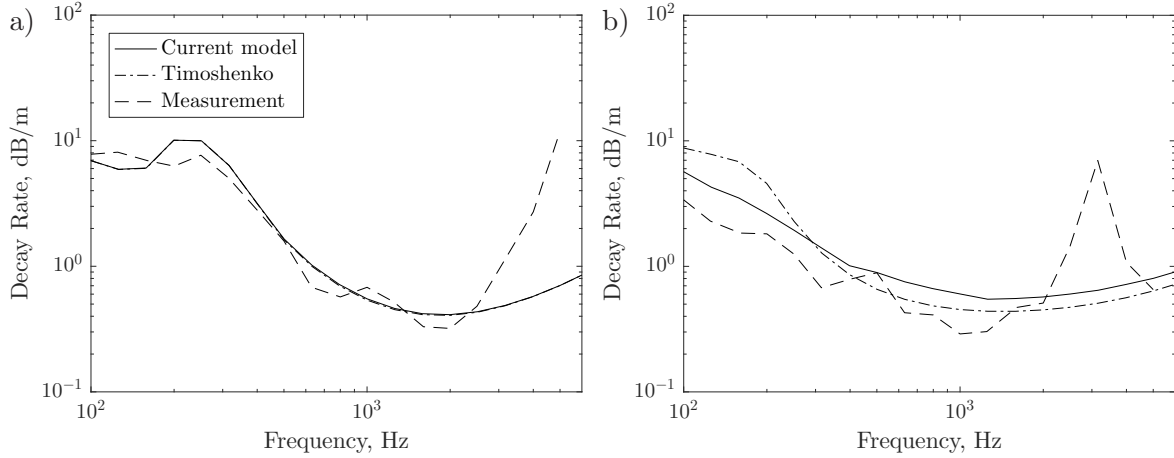


Figure 13: Track decay rate comparison against measurements for test track (a) vertical; (b) lateral

For the vertical direction, the current beam model and the Timoshenko beam model match exactly. For the lateral direction, at low frequencies, the presented beam model provides a better comparison with the results. Instead, between 300 Hz and 2 kHz the Timoshenko beam model shows a better agreement.

The cross mobility of the track is shown in Fig. 14, when the rail is excited vertically with an offset of 10 and 20 mm, i.e. at positions 3 and 4 respectively in Fig. 1. The lateral response for both graphs was measured at position 2. The cross mobility for the Timoshenko beam model is again based on the geometrical average of the vertical and lateral receptances as in Eq. (33). Fitting the cross mobility to the model, the factor was -14 dB for an offset of 10 mm (Fig. 14(a)) and -8 dB for an offset of 20 mm (Fig. 14(b)).

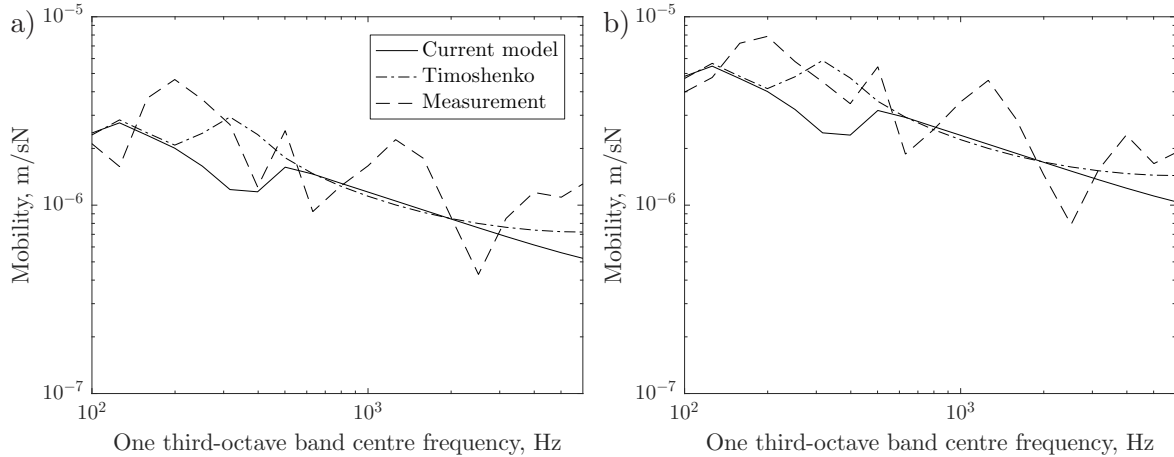


Figure 14: Cross mobility comparisons against measurements for test track (a) +10 mm offset ($X_{dB} = -14$ dB); (b) +20 mm offset ($X_{dB} = -8$ dB)

Here, agreement between the two models and the measurements is more limited although

the main trends are captured. Although neither model accounts for cross-sectional deformations, the predictions based on the empirical relationship of Eq. (33) also lack of information about the torsional behaviour of the rail, which has been shown to be essential to describe the lateral mobility.

5. Conclusions

An improved semi-analytical model for predicting the vibration of a railway track has been presented. The effects of torsion, shear centre eccentricity, warping and foundation eccentricity have been included. The model has been validated for the case of both a free and supported rail against a FE and a WFE model, providing excellent agreement for the dispersion up to 2 kHz. For a supported rail, results for the track decay rate and point mobility are presented for both vertical and lateral excitation. Of the various effects considered, compared with a Timoshenko beam the inclusion of torsion in the model has the greatest effect on the response in both the vertical and lateral directions. In order to improve the model further for frequencies above 2 kHz, consideration would need to be given to the cross-sectional deformation which is especially significant for the lateral response.

The forced response is also compared with the WFE results. Overall the model is shown to give excellent agreement with the WFE predictions up to 4 kHz for the vertical direction. For the lateral direction the agreement is good up to about 6 kHz at the centre of the rail head. With an offset of 20 mm, the forced response in both the vertical and lateral directions shows a good agreement up to about 1.4 kHz, above which the cross-sectional modes influence the response. For the axial direction the agreement is good over the whole frequency range. The cross mobility is also shown to give a good agreement up to about 1 kHz, above which higher order lateral waves influence the response. Compared with the empirical equation used for the classical Timoshenko beam model, this model provides a direct way of calculating the cross mobility.

Finally, from a comparison with measurements performed on a test track, it is seen that, by performing a curve fitting, the proposed model yields significantly different estimates of the lateral pad stiffness of the track, compared with the classical Timoshenko beam model. Again the effects of including torsion and rail pad eccentricity seem to be most influential for fitting the lateral mobility. The predicted cross mobility has more limited agreement, although the main trends are captured.

Acknowledgements

This work has been sponsored by Network Rail and the Engineering and Physical Sciences Research Council under the grant reference 1342762. All data published in this paper are openly available from the University of Southampton repository at: <http://doi.org/10.5258/SOTON/404573>.

References

- [1] N. Vincent, P. Bouvet, D.J. Thompson, and P.E. Gautier. Theoretical optimization of track components to reduce rolling noise. *Journal of Sound and Vibration*, 193(1): 161–171, 1996. DOI:10.1006/jsvi.1996.0255.
- [2] K.L. Knothe and S.L. Grassie. Modelling of railway track and vehicle/track interaction at high frequencies. *Vehicle System Dynamics*, 22(3-4):209–262, 1993. DOI:10.1080/00423119308969027.
- [3] S.L. Grassie, R.W. Gregory, and K.L. Johnson. The dynamic response of railway track to high frequency lateral excitation. *Journal of Mechanical Engineering Science*, 24(2): 91–95, 1982. DOI:10.1243/JMES.
- [4] D.J. Thompson and N. Vincent. Track Dynamic Behaviour at High Frequencies. Part 1: Theoretical Models and Laboratory Measurements. *Vehicle System Dynamics*, 24 (sup1):86–99, 1995. DOI:10.1080/00423119508969617.
- [5] N. Vincent and D.J. Thompson. Track Dynamic Behaviour at High Frequencies. Part 2: Experimental Results and Comparisons with Theory. *Vehicle System Dynamics*, 24 (sup1):100–114, 1995. DOI:10.1080/00423119508969618.
- [6] D.J. Thompson, B. Hemsworth, and N. Vincent. Experimental validation of the TWINS prediction program for rolling noise Part 1: Description of the model and method. *Journal of Sound and Vibration*, 193(1):123–135, 1996. DOI:10.1006/jsvi.1996.0252.
- [7] T.X. Wu and D.J. Thompson. A double Timoshenko beam model for vertical vibration analysis of railway track at high frequencies. *Journal of Sound and Vibration*, 224(2): 329–348, 1999. DOI:10.1006/jsvi.1999.2171.
- [8] T.X. Wu and D.J. Thompson. Analysis of lateral vibration behavior of railway track at high frequencies using a continuously supported multiple beam model. *The Journal of the Acoustical Society of America*, 106(3):1369–1376, 1999. DOI:10.1121/1.427171.
- [9] D.J. Thompson. Wheel-rail noise generation, part III: Rail vibration. *Journal of Sound and Vibration*, 161(3):421–446, 1993. DOI:10.1006/jsvi.1993.1084.
- [10] D.J. Mead. A general theory of harmonic wave propagation in linear periodic systems with multiple coupling. *Journal of Sound and Vibration*, 27:235–260, 1973. DOI:10.1016/0022-460X(73)90064-3.
- [11] K.L. Knothe, Z. Strzyzakowski, and K. Willner. Rail vibrations in the high frequency range. *Journal of Sound and Vibration*, 169(1):111–123, 1994. DOI:10.1006/jsvi.1994.1009.
- [12] L. Gavrić. Computation of propagative waves in free rail using a finite element technique. *Journal of Sound and Vibration*, 185:531–543, 1995. DOI:10.1006/jsvi.1995.0398.

- [13] J. Ryue, D.J. Thompson, P.R. White, and D.R. Thompson. Investigations of propagating wave types in railway tracks at high frequencies. *Journal of Sound and Vibration*, 315(1-2):157–175, 2008. DOI:10.1016/j.jsv.2008.01.054.
- [14] C.M. Nilsson, C.J.C. Jones, D.J. Thompson, and J. Ryue. A waveguide finite element and boundary element approach to calculating the sound radiated by railway and tram rails. *Journal of Sound and Vibration*, 321(3-5):813–836, 2009. DOI:10.1016/j.jsv.2008.10.027.
- [15] L. Gry. Dynamic modelling of railway track based on wave propagation. *Journal of Sound and Vibration*, 195:477–505, 1996. DOI:10.1006/jsvi.1996.0438.
- [16] A. Bhaskar, K.L. Johnson, G.D. Wood, and J. Woodhouse. Wheel-rail dynamics with closely conformal contact. Part 1: dynamic modelling and stability analysis. *Proceedings of the Institution of Mechanical Engineers Part F: Journal of Rail and Rapid Transit*, 211:11–26, 1997. DOI:10.1243/0954409971530860.
- [17] B. Ripke and K. Knothe. Die unendlich lange Schiene auf diskreten Schwellen bei harmonischer Einzellasterregung. *Fortschritt-Berichte VDI*, Reihe 11(Nr. 155), 1991.
- [18] B. Betgen, G. Squicciarini, and D.J. Thompson. On the prediction of rail cross mobility and track decay rates using Finite Element Models. In *Proceedings of the 10th European Congress and Exposition on Noise Control Engineering (EURONOISE2015)*, pages 2019–2024, Maastricht, Netherlands, 2015. EAA-NAG-ABAV.
- [19] M-Y. Kim, S-B. Kim, and N-I. Kim. Spatial stability of shear deformable curved beams with non-symmetric thin-walled sections. I: Stability formulation and closed-form solutions. *Computers and Structures*, 83:2525–2541, 2005. DOI:10.1016/j.compstruc.2005.07.003.
- [20] D.J. Thompson. *Railway noise and vibration: mechanisms, modelling and means of control*. Elsevier Science, Oxford, UK, 2009.
- [21] E. J. Sapountzakis and V. J. Tsipiras. Shear deformable bars of doubly symmetrical cross section under nonlinear nonuniform torsional vibrations application to torsional postbuckling configurations and primary resonance excitations. *Nonlinear Dynamics*, 62(4):967–987, 2010.
- [22] V. G. Mokos and E. J. Sapountzakis. Secondary torsional moment deformation effect by BEM. *International Journal of Mechanical Sciences*, 53(10):897–909, 2011.
- [23] A.S. Gendy and A.F. Saleeb. Vibration analysis of coupled extensional/flexural/torsional modes of curved beams with arbitrary thin-walled sections. *Journal of Sound and Vibration*, 174(2):261–274, 1994. DOI:10.1006/jsvi.1994.1275.

- [24] D.J. Thompson, W.J. Van Vliet, and J.W. Werheij. Developments of the indirect method for measuring the high frequency dynamic stiffness of resilient elements. *Journal of Sound and Vibration*, 213(1):169–188, 1998.
- [25] COMSOL Multiphysics. *COMSOL 4.4*. COMSOL AB., Stockholm, Sweden, 2013.
- [26] F. Tisseur and K. Meerbergen. The quadratic eigenvalue problem. *SIAM Review*, 43(2):235–286, 2001. DOI:10.1137/S0036144500381988.
- [27] D.J. Thompson. Experimental analysis of wave propagation in railway tracks. *Journal of Sound and Vibration*, 203(5):867–888, 1997. DOI:10.1006/jsvi.1997.0903.
- [28] J.R. Kuttler and V.G. Sigillito. On curve veering. *Journal of Sound and Vibration*, 75(4):585–588, 1981. DOI:10.1016/0022-460X(81)90448-X.
- [29] N.C. Perkins and C.D. Mote. Comments on curve veering in eigenvalue problems. *Journal of Sound and Vibration*, 106(3):451–463, 1986. DOI:10.1016/0022-460X(86)90191-4.
- [30] D.A. Wunsch. *Complex variables with applications*. Pearson Addison-Wesley, 2006.
- [31] British Standards Institution. BS EN 15461:2008+A1:2010: Railway applications - Noise emission - Characterization of the dynamic properties of track selections for pass by noise measurements, 2010.
- [32] C.J.C. Jones, D.J. Thompson, and R.J. Diehl. The use of decay rates to analyse the performance of railway track in rolling noise generation. *Journal of Sound and Vibration*, 293(3-5):485–495, 2006. DOI:10.1016/j.jsv.2005.08.060.